ROYAL SOCIETY
OF CHEMISTRY

PAPER

Check for updates

Ultrapermeable nanofiltration membranes with tunable selectivity fabricated with polyaniline nanofibers†

Chenhao Ji,[abc] Cheng-Wei Lin,[b] Shenghao Zhang,[c] Yaoli Guo,[a] Zhe Yang,[ac] Weiping Hu,[c] Shuangmei Xue,*[abc] Q. Jason Niu [ID] *[ac] and Richard B. Kaner [ID] *[b]

Ultrapermeable polyamide nanofiltration membranes with tunable salt sieving properties were prepared using polyaniline nanofibers. The structural evolution of the three-layered thin film composites enables the formation of both ultrathin and nanostructured polyamide selective layers on a macroporous microfiltration membrane for improved water permeance, while the acid doping chemistry of polyaniline endows the polyamide layer with tunable pore size and surface charge for improved ion sieving. The membrane with a confined pore size in the polyamide layer shows selectivities of 30.1 for Mg^{2+}/Na^+ and 279.0 for SO_4^{2-}/Cl^- with a high water permeance of 39.1 L m^{-2} h^{-1} bar^{-1}. The membrane with an enlarged pore size in the polyamide layer demonstrates an ultrahigh water permeance of 49.7 L m^{-2} h^{-1} bar^{-1} with good retention for both Na_2SO_4 and $MgSO_4$ which equals 98.7% and 97.9% salt rejection, respectively.

1. Introduction

Water scarcity is a chronic issue facing arid regions that restricts industrial development and quality of life.[1,2] Membrane technology offers a solution with high selectivity, high efficiency, and low energy consumption, which has been widely applied in desalination and wastewater treatment for providing fresh water beyond the hydrological cycle.[3,4] Nanofiltration (NF) is a membrane-based separation process with precise nanosized molecular sieving capability and mild operating conditions.[5] NF membranes with different molecular weight cut-offs (MWCO) are designed for increasingly important industrial applications, such as monovalent and divalent salt screening,[6,7] molecular weight-based sieving of organics,[8–10] and concentration of high value-added materials.[11]

Thin-film composite (TFC) membranes are the most widely used membrane structures for reverse osmosis (RO),[12–14] forward osmosis (FO), NF[15] and gas separation.[16,17] They normally contain a thin (∼100 nm) selective layer and a porous support layer, both of which are vitally important for the separation properties.[18] For an NF membrane, the defect-free and

highly permeable selective layer can be readily fabricated by interfacial polymerization. Reacting diamines with acyl chlorides enables the formation of a highly crosslinked aromatic polyamide (PA) film at the interface of two immiscible solvents. The thickness,[19] nanoscale morphology,[20] charge,[21,22] and microporosity[23–26] of the interfacially polymerized PA layers can greatly affect the NF performance. Extensive efforts have been made to develop next-generation NF membranes that possess excellent separation performance and high application feasibility.[27,28]

A better understanding of the reaction mechanism can provide guidance for the fabrication of highly permeable selective layers. However, due to the rapid formation (within 30 seconds) of an ultrathin PA film with a crosslinked molecular structure, the understanding of how reaction conditions systematically affect the formation of a PA layer of an NF membrane remains unclear. Multiple factors such as reaction kinetics, solute diffusion, phase separation, *etc.*, contribute to the complexity of interfacial polymerization.[29–31] For example, Zhang *et al.*[5] demonstrated that creating diffusion-driven instability with a piperazine (PIP) monomer generates Turing structures on the resulting PA layer. The structural evolution of the PA layer was also made possible by Jin *et al.*[32] through a strategy using a nano-templated sacrificial interlayer. These methods have resulted in tremendous increases in water permeance.

Polyaniline (PANI) is a conjugated polymer with repeating amine and imine moieties,[33] that tends to spontaneously form 1D nanostructures due to π–π stacking.[33,34] Different from other 1D nanofibrous materials, the conjugated backbone of PANI

[a]College of Civil and Transportation Engineering, Shenzhen University, Shenzhen 518060, China. E-mail: xueshuangmei999@gmail.com; qjasonniu@szu.edu.cn

[b]Department of Chemistry and Biochemistry and California NanoSystems Institute, University of California, Los Angeles, California 90095, USA. E-mail: kaner@chem.ucla.edu

[c]Institute for Advanced Study, Shenzhen University, Shenzhen 518060, China

† Electronic supplementary information (ESI) available. See DOI: 10.1039/d1ta10898k
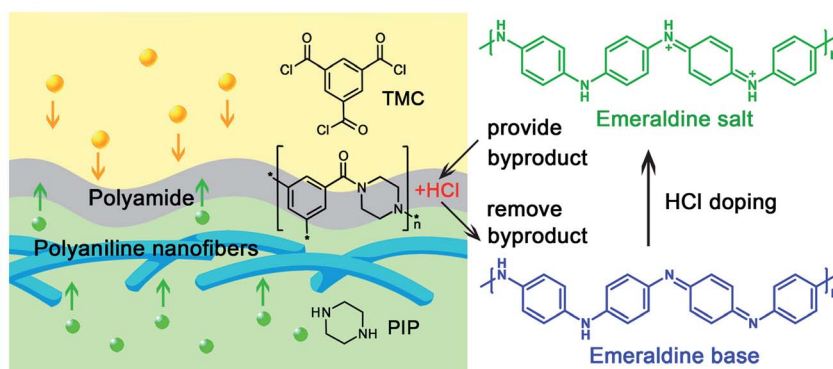
Fig. 1 Illustration of how the PANI interlayer works.

can be reversibly doped by acids and dedoped by bases to switch between the emeraldine salt and emeraldine base states.[35] Coincidentally, hydrochloric acid, that if often used in the doping of PANI, is also the byproduct of the interfacial polymerization of PA. This means that a nanofibrous PANI layer presented during interfacial polymerization may regulate the properties of the resulting PA layer from the perspective of chemical reaction kinetics. Although PANI has been used as an additive for fabricating mixed matrix membranes which show superior antifouling properties and pH-responsive selectivity,[36–38] the influence of the doping chemistry of PANI for preparing a PA thin film composite membrane has not been discussed previously.

We propose that interfacial polymerization can be modulated in the presence of PANI nanofibers by considering that the emeraldine base form of PANI can bond with protons to become the emeraldine salt form. In this work, a PA NF membrane with a tunable sieving ability was obtained by doping PANI nanofibers, as depicted in Fig. 1. The key factors (cross-linking density, thickness, surface charge, and pore size distribution) of the resulting selective layers can be readily tuned by the doping conditions of PANI interlayers leading to the controllable salt sieving ability of the resulting membrane. Meanwhile, the mutual stacking of nanofibrous PANI between a selective layer and a macroporous support layer creates a structure that give the membranes ultrahigh water permeance ranging from 39.7 to 49.7 L m^{-2} h^{-1} bar^{-1}, depending on the pore size of the PA selective layer.

2. Experimental

2.1 Synthesis of PANI nanofibers

PANI nanofibers were synthesized according to our previous work for nanofiber growth without shaking or stirring.[39] First, 0.3 mL of aniline was pipetted into a 20 mL glass vial and mixed with 10 mL of 1.0 M HCl solution. Next 0.18 g of ammonium persulfate was dissolved in another 10 mL of 1.0 M HCl solution. Then the ammonium persulfate solution was quickly poured into the aniline solution, slightly swirled for a few seconds to ensure a homogeneous mixture of the precursors and left still for 2 hours. After the undisturbed growth of the

PANI nanofibers, the resulting solution was sealed in a dialysis bag (cellulose acetate, MWCO = 10 000) and dialyzed against 5 mM HCl solution for 24 hours. During the dialysis, 5 mM of fresh HCl solution was replaced every 8 hours. After cleaning the unreacted reactants and oligomers, the PANI nanofiber solution was collected and stored in a 20 mL vial. All the chemicals unless specially noted were obtained from Sigma Aldrich, 1.0 M HCl solution was prepared by diluting 37% hydrochloric acid (AR grade, Sinopharm), DI water was supplied in our lab by a pilot two-stage reverse osmosis device.

2.2 Fabrication of the PANI interlayer

The as-synthesized PANI nanofibers were diluted with 5 mM HCl solution and DI water to prepare the emeraldine salt and emeraldine base PANI solutions with a concentration of 10 mg mL^{-1}. Polyethersulfone (PES) microfiltration (MF) membranes with an average pore size of 0.45 μm were used as the support membrane. A PES ultrafiltration (UF) membrane with a molecular weight cut-off of 50 000 Da was also used as a support membrane for comparison. The PANI interlayers were built with controlled loading by vacuum filtration and thermal annealing. The PANI solution was tip-sonicated for 5 min and stirred for 2 hours to ensure a homogeneous distribution before use. Controlled volumes of emeraldine base and emeraldine salt PANI nanofiber solutions were filtrated through the PES support membranes cut into a surface area of 14 cm^2, leaving the PANI nanofibers retained and mutually stacked on the support membrane to form the nanofibrous PANI interlayers.[10] The thickness of the PANI interlayers were controlled by varying the areal loading of the PANI nanofibers from 2 mg cm^{-2} to 5 mg cm^{-2}, 10 mg cm^{-2} and then to 20 mg cm^{-2}.

2.3 Fabrication of the composite membranes

Interfacial polymerization was carried out on the PANI covered PES membranes. The surface and cross-sectional morphology of an MF membrane is provided in Fig. S1.† The resulting composite was sandwiched between Teflon modules, and PIP solutions with two different concentrations (1% w/v and 0.05% w/v) were used as the aqueous phase. Each PIP solution was decanted onto the PANI layer and left still for 3 min, then the

This journal is © The Royal Society of Chemistry 2022

J. Mater. Chem. A, 2022, **10**, 4392–4401 | **4393**

PIP solution was removed, and the PANI layer surface was swept with compressed air to clean off the water droplets. A trimesoyl chloride (TMC) hexane solution (0.15% w/v) was subsequently poured onto the PANI layer and reacted with the aqueous phase for 30 s. After removing the TMC solution, the nascently formed PA layer was washed with hexane to remove the monomers and oligomers followed by a heat treatment at 80 °C for 5 min. The control TFC membranes without interlayers were also prepared by direct interfacial polymerization on the PES support membrane following the procedures above, with a 1% w/v PIP, and denoted as TFC-C. D/U-iTFC-1%/0.05% was used to depict the interlayered thin film composite (iTFC) membranes, where the prefixes D and U respectively stand for 'Doped' or 'Undoped', and the suffixes 1% or 0.05% represent the PIP solution concentrations used in the interfacial polymerization.

2.4 Characterizations

The membrane morphology was characterized using a scanning electron microscope (SEM, Nova NanoSEM450, FEI, USA). The nanostructures and the thickness of the selective layers were measured using an atomic force microscope (AFM, FastScan, Bruker, USA) with *ScanAsyst* Air mode. The AFM data were further processed by *Nanoscope Analysis* for analyzing the surface properties. An X-ray photoelectron spectrometer (XPS, K-Alpha, Thermo Scientific, USA) was employed to identify the chemical compositions of the PA selective layers. An SEM with a built-in energy-dispersive X-ray spectrometer (EDX) was utilized to characterize the elemental distribution of the prepared samples. A contact angle meter (DSA25E, Krüss, Germany) and a streaming potential analyzer (SurPASS, Anton Paar, Austria) were used to measure the surface hydrophilicities and charge properties of the PA layers, respectively.

2.5 Performance evaluation

A crossflow setup was used to evaluate the membrane performance. As shown in Fig. S2,† the crossflow device has four membrane testing cells, each has an effective testing area of 1.77 cm^2. The operational temperature was controlled at 25 °C by a built-in convective heat exchanger. Each run of the test used 1.0 L of 2000 ppm salt solution containing Na$_2$SO$_4$, MgSO$_4$, MgCl$_2$, NaCl or CaCl$_2$, respectively. The operational pressure was set at 0.5 MPa and each membrane was initially compressed at this pressure for 15 min before recording the permeance (J_w, L m^{-2} h^{-1} bar^{-1}) and the conductivity of the permeate (μS cm^{-1}). Eqn (1) describes the calculation of permeance in which Q stands for the permeate volume (L), P denotes the operational pressure (bar), and A is the membrane testing area which consistently equals 1.77 cm^2 as mentioned above.

$$J_w = \frac{Q}{P A \Delta t} \tag{1}$$

Single salt rejection R was recorded using eqn (2) in which C_p stands for the conductivity of the permeate and C_f is the conductivity of the feed solution. The solution conductivities were measured by an electric conductivity meter (B-771, Kyoto, Japan).

$$R = \left(1 - \frac{C_p}{C_f}\right) \times 100\% \tag{2}$$

Mixed salt solutions with equal molar quantities of Na$_2$SO$_4$ and NaCl and a total salt concentration of 2000 ppm was used to measure the anion selectivity (α^-) to SO$_4{}^{2-}$/Cl$^-$ of the prepared membranes, while the cation selectivity (α^+) to Mg^{2+}/Na$^+$ was measured using a salt solution with equal molar amounts of MgCl$_2$ and NaCl$_2$. The anion and cation selectivity were calculated based on eqn (3), where C_p and C_f stand for the ion concentrations in the feed and permeate solutions, respectively, as measured by an ion chromatograph (ICS-5000, Thermo-Fisher, USA).

$$\alpha^- = \frac{C_p(Cl^-)/C_p(SO_4{}^{2-})}{C_f(Cl^-)/C_f(SO_4{}^{2-})} \quad \alpha^+ = \frac{C_p(Na^+)/C_p(Mg^{2+})}{C_f(Na^+)/C_f(Mg^{2+})} \tag{3}$$

Solutions containing 0.5 g L^{-1} polyethylene glycol (PEG) with molecular weights from 200 to 800 Da were used to test the molecular weight cut-off (MWCO) of the NF membranes. The concentrations of the PEG solutions were measured by a total organic carbon analyzer (TOC, model TOCVPN, Shimadzu, Japan), while the Stokes diameters (d_s) of the PEGs were calculated using eqn (4):

$$d_s = 33.46 \times 10^{-3} \times M^{0.557} \tag{4}$$

Based on eqn (4), the equivalent pore radius distributions of the PA selective layers were calculated according to eqn (5). Specifically, the PEG rejection of each membrane was plotted as a function of the PEG molecular weight, while the format of the x-axis and y-axis were respectively changed to logarithmic and probability coordinates; the y values were found when x equals 50% and defined as μ_p, at the same time, σ_p was defined as $R_{84.13\%}/R_{50\%}$. The values of μ_p and σ_p for each membrane were then calculated and substituted into eqn (5) to obtain the pore size distribution of each membrane.

$$\frac{df(d_p)}{d(d_p)} = \frac{1}{d_p \ln \sigma_p \sqrt{2\pi}} \exp\left[-\frac{(\ln d_p - \ln \mu_p)^2}{2(\ln \sigma_p)^2}\right] \tag{5}$$

3. Results and discussion

3.1 Nanofibrous PANI interlayers

The morphology of the synthesized PANI nanofibers is presented in Fig. S3.† The PANI nanofibers were stacked on a PES MF membrane by vacuum filtration, and a series of PANI interlayers with loadings from 2 mg cm^{-2} to 20 mg cm^{-2} were prepared for comparing the resulting composite structure (Fig. S4†). A low loading of polyaniline nanofibers results in the formation of an incomplete polyaniline interlayer while a high loading causes additional permeation resistance. A loading of

4394 | *J. Mater. Chem. A*, 2022, **10**, 4392–4401

This journal is © The Royal Society of Chemistry 2022

10 mg cm^{-2} created an intact PANI interlayer with controlled thickness around 720 nm and was therefore used for the following experiments. Previously reported works have demonstrated that a one-dimensional (1D) nanomaterial-based interlayer is an excellent candidate to promote the interfacial polymerization process and optimize the membrane structure. Fig. 2a and b indicate that the PANI nanofiber overlaid PES MF membrane has a reduced pore size and a confined pore size distribution compared to the neat one which is beneficial and crucial for interfacial polymerization to regulate the diffusion of PIP monomers.

We speculate that the emeraldine base PANI interlayer is the driving force to remove and capture the hydrochloric acid generated from the interfacial polycondensation reaction. To prove this concept, interfacial polymerizations were carried out both on undoped PANI interlayers and doped PANI interlayers for comparison. Considering that the aqueous monomer (PIP) is a basic organic compound that can neutralize the HCl byproduct, two different concentrations of PIP solutions (1% w/v and 0.05% w/v) were applied for better understanding of the interfacial polymerization process.

Doped PANI nanofibers appear emerald green (Fig. 2e), while undoped polyaniline nanofibers are blue (Fig. 2d). The change in color from blue to green indicates that the PANI nanofibers become doped during the interfacial polymerization. Fig. S5† presents the optical images showing the membrane fabrication process. As can be seen, when 1% w/v of PIP was used for interfacial polymerization, both doped and undoped PANI interlayers (Fig. S5a–c and g–i†) of the resulting membranes turn into the emeraldine base form of PANI because the HCl byproduct generated from the interfacial polymerization and dopants originally bonded in the PANI interlayer are neutralized by the excess PIP monomers. However, when a low PIP concentration, 0.05% w/v, was used for interfacial polymerization, the undoped PANI interlayer turns from blue to green (Fig. S5b, e and f†), indicating that the HCl byproduct generated

from the interfacial polymerization successfully protonated the PANI interlayer.

While the color changes of the PANI nanofibers offer some limited information, the electrical conducting nature of PANI could provide dynamic electrochemical analysis of the PANI interlayer during interfacial polymerization.[34] Therefore, we measured the *in situ* relative conductance of the PANI interlayers during interfacial polymerization using a 0.05% w/v PIP solution. As presented by Fig. 2c, a PANI modified MF membrane was sandwiched between two polyacrylic acid plates and connected to the electrochemistry analyzer. The polyacrylic acid plate facing the PANI layer was slotted for conducting interfacial polymerization. At the very beginning stage, the variations of conductance in both measurements follow a similar trend that of a very large increase followed by a gradual decrease. This is due to the high ionic conductance of the basic PIP solution. The impregnation of the PIP solution first helps the device form a relatively conductive circuit and then the circuit is gradually closed as the PIP solution further diffuses into the MF support membrane underneath.

The apparent differences occur when the TMC solution was added into the circuit at around 200 s of operation time. The doped PANI layer barely shows any difference in the conductance. In contrast, the undoped PANI layer shows a notable increase in conductance, which demonstrates that the undoped PANI layer can be doped by the byproduct HCl during interfacial polymerization. We believe the following decrease in conductance is due to the accumulated enthalpy from the condensation polymerization, which heats up the PANI interlayer and causes the de-doping.

We further calculated the system energy comprising water, HCl, PANI and PIP molecules as presented in Fig. S6.† The result is consistent with the concept that HCl will preferentially bond with PANI to form the most stable system with the lowest energy. From a mechanistic perspective, we have demonstrated that the undoped emeraldine base PANI interlayer can preferentially bond with HCl at a low PIP concentration, while the
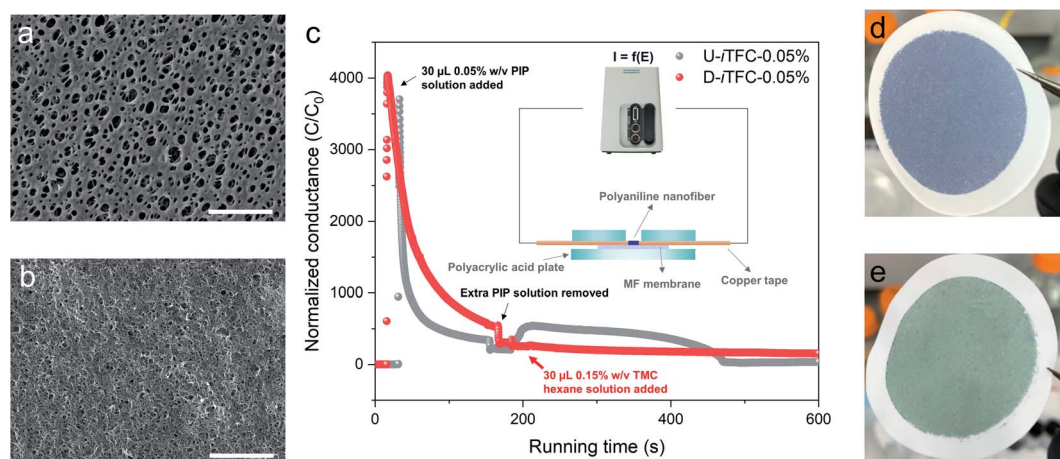

Fig. 2 Surface morphology of (a) a neat PES MF membrane and (b) a PANI nanofiber modified one. Scale bar: 5 μm, (c) *in situ* conductance measurement of the PANI layers during the interfacial polymerization process. (d) An emeraldine base and (e) an emeraldine salt PANI nanofiber layer on PES MF membranes.

This journal is © The Royal Society of Chemistry 2022

J. Mater. Chem. A, 2022, **10**, 4392–4401 | **4395**

doped emeralde salt PANI interlayer will offer extra HCl to the interfacial reaction system, thus slowing down the interfacial polymerization reaction.

3.2 Membrane morphology

Fig. 3 shows the morphologies of TFC-C, U-*i*TFC-1%, and U-*i*TFC-0.05% membranes. The *i*TFC membranes demonstrate a distinct three-layered composite structure with much rougher and crumpled PA layers. Direct interfacial polymerization of PIP and TMC on a MF membrane results in a dense, flat, and nodular PA layer (Fig. 3a and d) with an average roughness R_a equal to 4.28 nm as shown in Fig. 4a. In contrast, interfacial polymerization on an undoped PANI nanofibrous layer using both high (1% w/v) and low (0.05% w/v) PIP concentrations led to the formation of thinner PA films (as the underneath PANI interlayer can be readily observed) with crumpled nanostructures, as shown in Fig. 3b and e. The concentrations of the PIP monomer cause differences in the size of the nanostructures as can be seen by comparing Fig. 3e and f. The relatively high PIP concentration helps form a PA layer with tubular nanostructures with smaller sizes, whereas the low PIP concentration causes the formation of wider fine leaf-like nanostructures. On the other hand, the initial doping state of the PANI interlayers does not cause notable differences to the PA layer morphology when we compare the surface morphology of U-*i*TFC-1% and U-*i*TFC-0.05% with D-*i*TFC-1% and D-*i*TFC-0.05% (Fig. S7†). We believe the differences in size can be mainly ascribed to the reaction kinetics of the interfacial polymerization.

The interfacial reaction of PIP and TMC is a diffusion-limited process because the size of the PIP molecules is small enough to pass through the PA layer initially formed by itself and TMC.[29]

This means that a higher PIP concentration will lead to a higher reaction rate for the interfacial polymerization when the other reaction conditions are kept constant. Therefore, the initially formed nanostructures on the PA layer will be more quickly covered and flattened by the later formed PA moieties at a higher PIP concentration. Additionally, the interactions between the PANI interlayers and PIP also participate in the diffusion process. The hydrogen bonds formed between the nanofibrous PANI and PIP reduce the diffusion rate and increase the inhomogeneity in the diffusion direction. This not only assists the formation of crumpled nanostructures on the PA layer, but also reduces the thickness of the PA film.

The thickness of PA films loaded onto silicon wafers was measured by AFM (Fig. S8†). The height differences across the silicon wafers and the PA films noted by the yellow lines were measured and the resulting film thicknesses are shown in Fig. 4b. PA layers prepared on PANI interlayers demonstrate a reduced film thickness when we compare the thicknesses of TFC-C, U-*i*TFC-1% and D-*i*TFC-1% which were made with the same PIP concentrations. This result corroborates that the interaction between PIP and PANI can reduce the diffusion rate of the PIP monomers during the interfacial polymerization. Further lowering the PIP concentration helps achieve the thinnest PA film thickness – down to 11 nm (D-*i*TFC-0.05%). In the cases of both 1% w/v and 0.05% w/v PIP, the doped PANI interlayer produces thinner PA layers, owing to the decelerated interfacial polymerization reaction rate.

Previous research has demonstrated that both the heterogeneous diffusion of PIP and the structural template effect of the interlayer cause the formation of PA layers with crumpled nanostructures. Here, we mainly ascribe the formation of such nanostructures to the uneven distribution of PANI moieties at
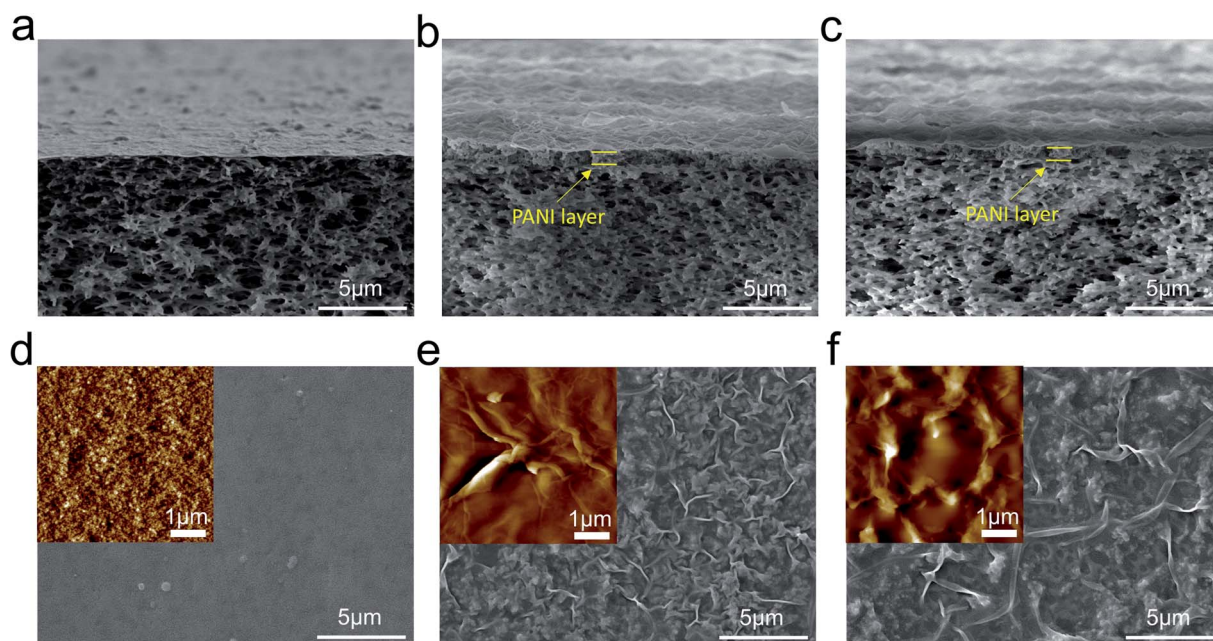

Fig. 3 Surface and cross-sectional morphology of (a and d) TFC–C, (b and e) U-*i*TFC-1%, and (c and f) U-*i*TFC-0.05%, inset with the corresponding AFM images.
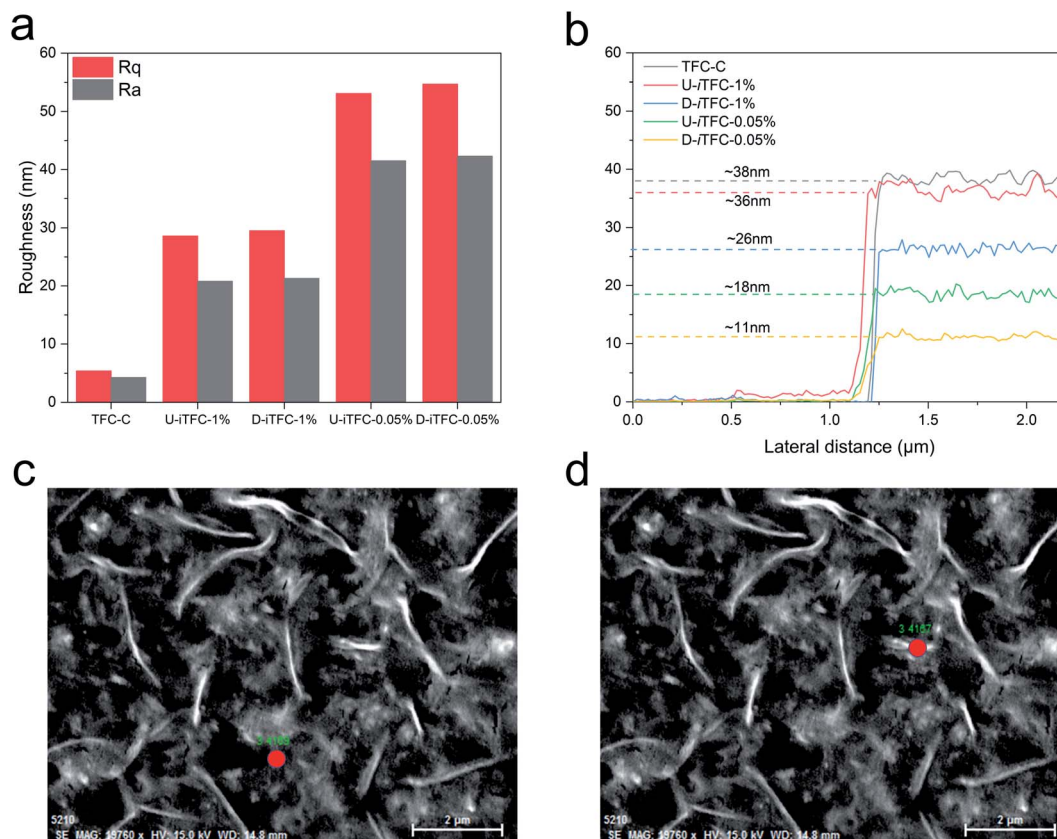
4396 | *J. Mater. Chem. A*, 2022, **10**, 4392–4401

This journal is © The Royal Society of Chemistry 2022

Fig. 4 (a and b) Surface roughness and thickness measured by AFM. Surface images of U-*i*TFC-1% for measuring the elemental compositions marked as the red dots. The nitrogen elemental content of points in (c) and (d) are 5.78% and 7.46%, respectively.

the nanoscale. The stacking of PANI nanofibers causes the PANI-rich and pore-rich regions on the resulting interlayer. EDX was employed to analyze the elemental composition of the ridge and valley positions of U-*i*TFC-1% as shown in Fig. 4, with the results presented in Fig. S9, Tables S1 and Table S2.† The ridge on the PA layer (Fig. 4d) exhibits an obviously higher nitrogen content (7.46% *versus* 5.78%) than the valley (Fig. 4c). This result demonstrates that the formation of crumpled nanostructures of the PA layer mainly occurs on the PANI-rich spots of the PANI interlayer and is caused by an integration of factors including the monomer diffusion, a template effect, and the hydrophilicity of the nanofibrous interlayer.

3.3 Surface properties

Tailoring the kinetics of interfacial polymerization not only affects the morphology of the PA selective layer, but also changes the key surface properties of the membranes. The pore size distribution, hydrophilicity, and surface charge properties of the membranes are presented in Fig. 5. Generally, the PA layers prepared on doped PANI interlayers exhibit superior surface properties for both hydrophilicity and zeta potential, highlighting the advantages of using PANI for designing nanofiltration membranes. A series of PEGs with different molecular weights were used to analyze the molecular weight cut-off (MWCO) and calculate the pore size distribution of the

PA selective layer (Fig. 5a). Differing from the other membranes, U-*i*TFC-1% has a much lower MWCO of ~230 Da and a narrow pore size distribution centered at 0.35 nm. It shows that the undoped PANI facilitates the formation of a more uniform PA with a higher cross-linking density during interfacial polymerization. This phenomenon has rarely been seen in previously reported works, because most nanofibrous interlayers only provide structural and hydrophilicity enhancement to the support membrane, but seldom show the ability to tune the microporosity of the resulting PA layer simultaneously.

In contrast to the undoped PANI, the MWCO for the PA layer built on doped PANI was increased from ~230 Da to ~434 Da at the same PIP concentration. For instance, the resulting PA layer of D-*i*TFC-1% possesses a broader pore size distribution with a more negative charge, and better hydrophilicity compared to U-*i*TFC-1%. The pre-doped PANI interlayer accelerates the protonation of the PIP monomers, resulting in many acyl chlorides from the TMC monomers remaining unreacted. These unreacted monomers are then hydrolyzed by water at the aqueous/organic interface and converted into carboxyl groups on the outer surface of the PA layer. This both reduces the reaction rate from a reaction kinetics perspective and the degree of crosslinking of the PA layer at a molecular scale. The impact of the doping chemistry of PANI nanofibers on the properties of the resulting PA layer become more prominent when a low PIP concentration is used. A looser selective layer can be further
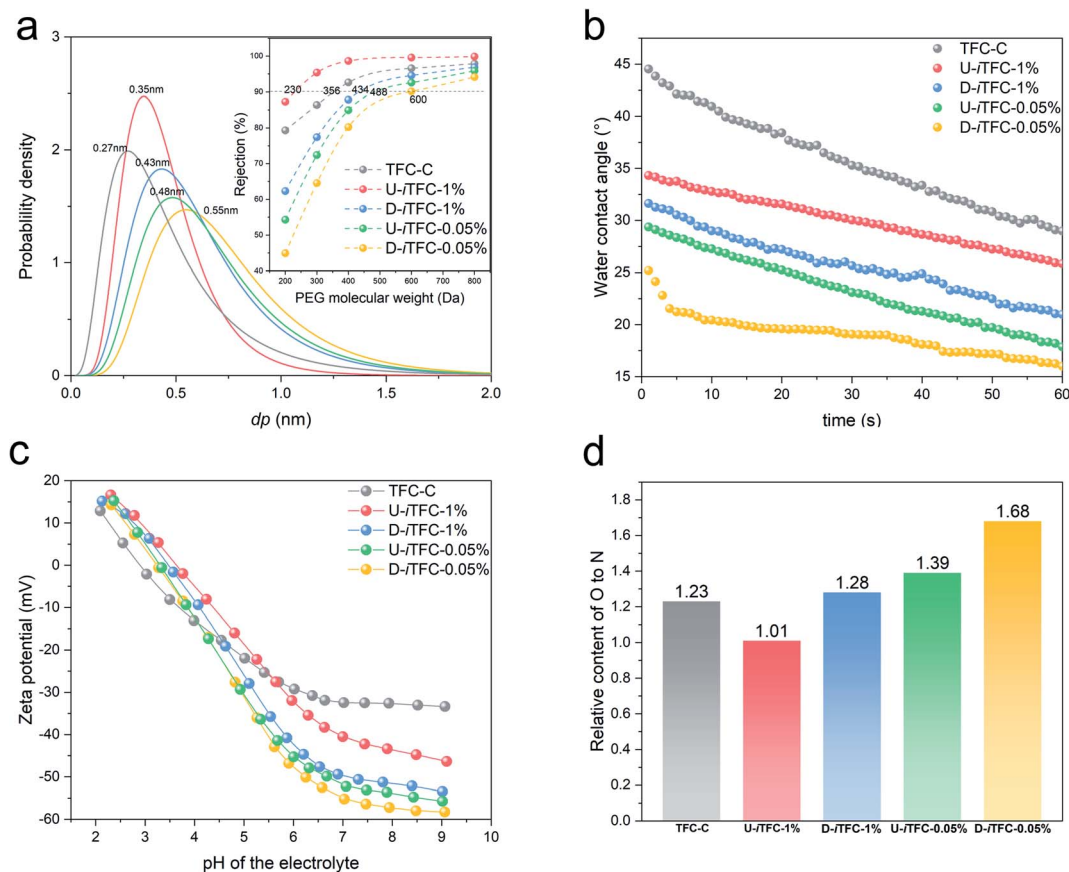
Fig. 5 Surface properties of the PA layers: (a) pore size distribution, (b) dynamic water contact angle, (c) zeta potential, and (d) O/N ratio measured by XPS.

obtained by reducing the PIP concentration. Therefore, D-*i*TFC-0.05% exhibits the lowest MWCO, water contact angle and zeta-potential due to the loose molecular structure formed in the presence of doped PANI nanofibers.

The chemical composition of the NF membranes was analyzed by XPS. The O/N ratios and peak area in the C 1s spectra (Fig. S11†) are strongly related to the crosslinking density of the PA layer. In Fig. 5d, the O/N ratios of the membrane surfaces are in the sequence of U-*i*TFC-1% < TFC-C < D-*i*TFC-1% < U-*i*TFC-0.05% < D-*i*TFC-0.05%. This proves the aforementioned results that both acid doping of the PANI nanofibers and reducing the concentration of the aqueous monomer helps the formation of a less cross-linked PA selective layer with a thinner and more hydrophilic characteristic. Conversely, removing the byproduct HCl from the interfacial reaction through the acid binding nature of undoped PANI results in a thicker PA layer with increased crosslinking density. It is also worth noting that the nitrogen rich PANI interlayers of the *i*TFC membranes can interfere with the elemental analysis of the PA layers, causing a lower O/N ratio. However, the basic trend is still clear that the doping chemistry of PANI offers a facile control of the surface properties and microporosity of the PA selective layer, which contributes to a tunable sieving ability.

3.4 NF performance

Table 1 summarizes the results of the NF performance. The PANI nanofibers endow the resulting membranes with tunable sieving ability. Compared with the control, U-*i*TFC-1% with a thinner nanostructured PA layer and narrower pore size distribution shows superior water permeance and salt selectivity. The water permeance of U-*i*TFC-1% reaches 39.7 L m^{-2} h^{-1} bar^{-1} which is more than twice the control and approximately 1.5 times that of a sample prepared on a UF membrane using the same process. Additionally, U-*i*TFC-1% also demonstrates better salt rejection rates than U-*i*TFC-1%-UF. It is technically more difficult to form a nanofibrous interlayer with a uniform distribution of the nanofibers on an UF membrane than that on a MF membrane, which causes difficulties in the defect control of the PA layer.

The improvements in water permeance and salt rejection highlight the advantages of combining a nanofibrous interlayer with an MF membrane as the support.[40] The high water permeance is accompanied with a high selectivity for both Mg^{2+}/Na^{+} and SO$_4^{2-}$/Cl^{-} which equals 30.1 and 279.0, respectively. The hydrated radii of Na^{+}, Mg^{2+}, Ca^{2+}, Cl^{-}, and SO$_4^{2-}$ are 0.36, 0.43, 0.41, 0.33 and 0.38 nm, respectively. Therefore, the reduced and confined pore size of U-*i*TFC-1% features the high retention for multivalent ions due to size exclusion. But this

4398 | *J. Mater. Chem. A*, 2022, **10**, 4392–4401

This journal is © The Royal Society of Chemistry 2022

Table 1 NF Performance Evaluation of the *i*TFC Membranes

| Sample | PWF, L m^{-2} h^{-1} bar^{-1} | Salt rejection and selectivity | | | | | | Mixed salts solution | |
| | | Single salt solution (%) | | | | | | | |
		Na$_2$SO$_4$	MgSO$_4$	MgCl$_2$	CaCl$_2$	NaCl		α^+	α^-
TFC-C	18.6 ± 1.1	94.1 ± 1.7	90.9 ± 1.3	41.3 ± 2.7	32.8 ± 1.5	23.6 ± 1.4		1.3	13.1
U-*i*TFC-1%	39.1 ± 1.4	99.7 ± 0.3	98.7 ± 0.7	97.1 ± 0.7	93.1 ± 0.9	17.5 ± 1.7		30.1	279.0
D-*i*TFC-1%	40.7 ± 2.2	98.9 ± 0.7	97.2 ± 1.1	82.7 ± 2.1	74.2 ± 1.7	15.1 ± 1.9		5.2	78.4
U-*i*TFC-0.05%	47.5 ± 2.7	99.1 ± 0.4	98.1 ± 1.2	77.7 ± 1.5	56.3 ± 1.4	12.4 ± 1.7		3.8	98.5
D-*i*TFC-0.05%	49.7 ± 3.3	98.7 ± 0.5	97.9 ± 1.4	71.5 ± 1.3	49.1 ± 1.2	9.2 ± 1.5		3.4	70.2
Control samples prepared on PES UF membranes, TFC-C-UF and U-*i*TFC-1%-UF follow the same fabrication process of TFC-C and U-*i*TFC-1%, respectively									
TFC-C-UF	12.1 ± 0.4	98.3 ± 1.2	97.4 ± 1.4	53.6 ± 1.2	35.3 ± 0.7	28.8 ± 1.4		1.5	43.4
U-*i*TFC-1%-UF	26.2 ± 0.9	98.8 ± 1.4	97.8 ± 2.1	95.0 ± 1.2	90.2 ± 1.7	18.2 ± 1.3		17.8	75.2

pore size has much less capacity for retaining monovalent Na$^+$ and Cl$^-$ which also have smaller size and less charge to form enough electrostatic repulsion between the membrane and the hydrated ions. Therefore, the resulting membrane demonstrates high selectivity for differentiating Mg^{2+} and Na$^+$. As for negatively charged and multivalent sulfate ion, the synergistic size exclusion and electrostatic repulsion cutoff its transmembrane transport that forms an effective differentiation for SO$_4^{2-}$ and Cl$^-$.

Increased pore size, broad pore size distribution, and reduced thickness of the selective layer all promote better water permeance due to the reduced mass transfer barriers. This compromises the salt rejection for MgCl$_2$, CaCl$_2$ and NaCl, and therefore the selectivity for Mg^{2+}/Na$^+$ declined accordingly. However, the membranes still maintain a decently high rejection for Na$_2$SO$_4$ and MgSO$_4$, owing to the highly negatively charged surface of the PA selective layers plus the Donnan effect during membrane separation. Compared with the highly selective U-*i*TFC-1% which has advantages for recovery of specific salts and small organics, these ultrapermeable membranes would be better used for wastewater treatment containing heavy metal ions and organics with relatively larger molecular size.

Fig. S14† compares the Na$_2$SO$_4$ rejection and water permeance reported here with previous work[41–53] sorted by the materials used in the interlayer. The results indicate that the *i*TFC membrane with a nanofibrous PANI interlayer not only has a tunable sieving ability, but also demonstrates a superior integrated NF performance compared to the others built on polymeric, carbon, and microporous material-based interlayers.

4. Conclusions

A nanofibrous PANI interlayer enables the fabrication of ultrapermeable NF membranes with tunable sieving properties. The doping chemistry of PANI enables either removing or providing extra HCl for the interfacial reaction, thus controlling the pore size distribution and surface charge of the resulting PA layer by avoiding or imposing protonation to the

PIP monomers. This also regulates the thickness of the PA layer from the perspective of reaction kinetics. Using 1% w/v of PIP and an undoped PANI interlayer results in a reduced pore size and a confined pore size distribution of the PA layer, providing ultrahigh selectivity for both SO$_4^{2-}$/Cl$^-$ (279.0) and Mg^{2+}/Na$^+$ (30.1) with reasonable water permeance (39.1 L m^{-2} h^{-1} bar^{-1}). In contrast, using an ultralow concentration of PIP for interfacial polymerization with doped PANI interlayers results in the formation of an ultrathin (~11 nm) PA layer with a loose molecular structure and stronger negative charge. This creates extremely high water permeance (up to 49.7 L m^{-2} h^{-1} bar^{-1}) with good retention (98.7% and 97.9% for Na$_2$SO$_4$ and MgSO$_4$), respectively.

Conflicts of interest

There are no conflicts to declare.

Acknowledgements

References

1 M. A. Shannon, P. W. Bohn, M. Elimelech, J. G. Georgiadis, B. J. Marinas and A. M. Mayes, Science and technology for water purification in the coming decades, *Nature*, 2008, **452**(7185), 301–310.

2 J. R. Werber, C. O. Osuji and M. Elimelech, Materials for next-generation desalination and water purification membranes, *Nat. Rev. Mater.*, 2016, **1**(5), 16018.

This journal is © The Royal Society of Chemistry 2022

J. Mater. Chem. A, 2022, **10**, 4392–4401 | **4399**

3 M. Elimelech and W. A. Phillip, The Future of Seawater Desalination: Energy, Technology, and the Environment, *Science*, 2011, **333**, 712–717.

4 B. McVerry, M. Anderson, N. He, H. Kweon, C. Ji, S. Xue, E. Rao, C. Lee, C. W. Lin, D. Chen, D. Jun, G. Sant and R. B. Kaner, Next-Generation Asymmetric Membranes Using Thin-Film Liftoff, *Nano Lett.*, 2019, **19**(8), 5036–5043.

5 Z. Tan, S. Chen, X. Peng, L. Zhang and C. Gao, Polyamide membranes with nanoscale Turing structures for water purification, *Science*, 2018, **360**, 518–521.

6 P. Sarkar, S. Modak and S. Karan, Ultraselective and Highly Permeable Polyamide Nanofilms for Ionic and Molecular Nanofiltration, *Adv. Funct. Mater.*, 2020, **31**(3), 2007054.

7 S. M. Xue, Z. L. Xu, Y. J. Tang and C. H. Ji, Polypiperazine-amide Nanofiltration Membrane Modified by Different Functionalized Multiwalled Carbon Nanotubes (MWCNTs), *ACS Appl. Mater. Interfaces*, 2016, **8**(29), 19135–19144.

8 P. Gorgojo, S. Karan, H. C. Wong, M. F. Jimenez-Solomon, J. T. Cabral and A. G. Livingston, Ultrathin Polymer Films with Intrinsic Microporosity: Anomalous Solvent Permeation and High Flux Membranes, *Adv. Funct. Mater.*, 2014, **24**(30), 4729–4737.

9 S.-M. Xue, C.-H. Ji, Z.-L. Xu, Y.-J. Tang and R.-H. Li, Chlorine resistant TFN nanofiltration membrane incorporated with octadecylamine-grafted GO and fluorine-containing monomer, *J. Membr. Sci.*, 2018, **545**, 185–195.

10 C. Ji, S. Xue, C. W. Lin, W. H. Mak, B. T. McVerry, C. L. Turner, M. Anderson, J. C. Molas, Z. Xu and R. B. Kaner, Ultrapermeable Organic Solvent Nanofiltration Membranes with Precisely Tailored Support Layers Fabricated Using Thin-Film Liftoff, *ACS Appl. Mater. Interfaces*, 2020, **12**(27), 30796–30804.

11 S. Xu, J. Song, Q. Bi, Q. Chen, W.-M. Zhang, Z. Qian, L. Zhang, S. Xu, N. Tang and T. He, Extraction of lithium from Chinese salt-lake brines by membranes: design and practice, *J. Membr. Sci.*, 2021, **635**, 119441.

12 Z. Jiang, S. Karan and A. G. Livingston, Water Transport through Ultrathin Polyamide Nanofilms Used for Reverse Osmosis, *Adv. Mater.*, 2018, **30**(15), e1705973.

13 S. Karan, Z. Jiang and A. G. Livingston, Sub-10 nm polyamide nanofilms with ultrafast solvent transport for molecular separation, *Science*, 2015, **348**(6241), 1347–1351.

14 X.-H. Ma, Z.-K. Yao, Z. Yang, H. Guo, Z.-L. Xu, C. Y. Tang and M. Elimelech, Nanofoaming of Polyamide Desalination Membranes To Tune Permeability and Selectivity, *Environ. Sci. Technol. Lett.*, 2018, **5**(2), 123–130.

15 C. Ji, S. Xue, Y.-J. Tang, X.-H. Ma and Z.-L. Xu, Polyamide Membranes with Net-Like Nanostructures Induced by Different Charged MOFs for Elevated Nanofiltration, *ACS Appl. Polym. Mater.*, 2019, **2**(2), 585–593.

16 J. E. Cadotte *Interfacially synthesized reverse osmoss membrane*. 1979.

17 W. J. Koros and C. Zhang, Materials for next-generation molecularly selective synthetic membranes, *Nat. Mater.*, 2017, **16**(3), 289–297.

18 G. Gong, P. Wang, Z. Zhou and Y. Hu, New Insights into the Role of an Interlayer for the Fabrication of Highly Selective and Permeable Thin-Film Composite Nanofiltration Membrane, *ACS Appl. Mater. Interfaces*, 2019, **11**(7), 7349–7356.

19 M. R. Chowdhury, J. Steffes, B. D. Huey and J. R. McCutcheon, 3D printed polyamide membranes for desalination, *Science*, 2018, **361**(6403), 682–686.

20 Z. Zhai, C. Jiang, N. Zhao, W. Dong, H. Lan, M. Wang and Q. J. Niu, Fabrication of advanced nanofiltration membranes with nanostrand hybrid morphology mediated by ultrafast Noria–polyethyleneimine codeposition, *J. Mater. Chem. A*, 2018, **6**(42), 21207–21215.

21 S. Aguilar, S. Bustillos, S. Xue, C. H. Ji, W. H. Mak, E. Rao, B. T. McVerry, E. C. La Plante, D. Simonetti, G. Sant and R. B. Kaner, Enhancing Polyvalent Cation Rejection Using Perfluorophenylazide-Grafted-Copolymer Membrane Coatings, *ACS Appl. Mater. Interfaces*, 2020, **12**(37), 42030–42040.

22 B. Q. Huang, Y. J. Tang, Z. X. Zeng, S. M. Xue, C. H. Ji and Z. L. Xu, High-Performance Zwitterionic Nanofiltration Membranes Fabricated *via* Microwave-Assisted Grafting of Betaine, *ACS Appl. Mater. Interfaces*, 2020, **12**(31), 35523–35531.

23 M. F. Jimenez-Solomon, Q. Song, K. E. Jelfs, M. Munoz-Ibanez and A. G. Livingston, Polymer nanofilms with enhanced microporosity by interfacial polymerization, *Nat. Mater.*, 2016, **15**(7), 760–767.

24 Y. Liang, Y. Zhu, C. Liu, K. R. Lee, W. S. Hung, Z. Wang, Y. Li, M. Elimelech, J. Jin and S. Lin, Polyamide nanofiltration membrane with highly uniform sub-nanometre pores for sub-1 A precision separation, *Nat. Commun.*, 2020, **11**(1), 2015.

25 F. Foglia, S. Karan, M. Nania, Z. Jiang, A. E. Porter, R. Barker, A. G. Livingston and J. T. Cabral, Neutron Reflectivity and Performance of Polyamide Nanofilms for Water Desalination, *Adv. Funct. Mater.*, 2017, **27**(37), 1701738.

26 Z.-M. Zhan, Z.-L. Xu, K.-K. Zhu, S.-M. Xue, C.-H. Ji, B.-Q. Huang, C. Y. Tang and Y.-J. Tang, Superior nanofiltration membranes with gradient cross-linked selective layer fabricated *via* controlled hydrolysis, *J. Membr. Sci.*, 2020, **604**, 118067.

27 Z. Yang, H. Guo and C. Y. Tang, The upper bound of thin-film composite (TFC) polyamide membranes for desalination, *J. Membr. Sci.*, 2019, **590**, 117297.

28 B.-Q. Huang, Y.-J. Tang, Z.-X. Zeng and Z.-L. Xu, Microwave heating assist preparation of high permselectivity polypiperazine-amide nanofiltration membrane during the interfacial polymerization process with low monomer concentration, *J. Membr. Sci.*, 2020, **596**, 117718.

29 V. Freger, Nanoscale Heterogeneity of Polyamide Membranes Formed by Interfacial Polymerization, *Langmuir*, 2003, **19**, 4791–4797.

30 Z. Yang, P. F. Sun, X. Li, B. Gan, L. Wang, X. Song, H. D. Park and C. Y. Tang, A Critical Review on Thin-Film Nanocomposite Membranes with Interlayered Structure: Mechanisms, Recent Developments, and Environmental Applications, *Environ. Sci. Technol.*, 2020, **54**(24), 15563–15583.

4400 | *J. Mater. Chem. A*, 2022, **10**, 4392–4401

This journal is © The Royal Society of Chemistry 2022

31 C. Ji, Z. Zhai, C. Jiang, P. Hu, S. Zhao, S. Xue, Z. Yang, T. He and Q. J. Niu, Recent advances in high-performance TFC membranes: a review of the functional interlayers, *Desalination*, 2020, **500**, 114869.

32 Z. Wang, Z. Wang, S. Lin, H. Jin, S. Gao, Y. Zhu and J. Jin, Nanoparticle-templated nanofiltration membranes for ultrahigh performance desalination, *Nat. Commun.*, 2018, **9**(1), 2004.

33 C. W. Lin, S. Xue, C. Ji, S. C. Huang, V. Tung and R. B. Kaner, Conducting Polyaniline for Antifouling Ultrafiltration Membranes: Solutions and Challenges, *Nano Lett.*, 2021, **21**(9), 3699–3707.

34 D. Li, J. Huang and R. B. Kaner, Polyaniline Nanofibers: A Unique Polymer Nanostructure for Versatile Applications, *Acc. Chem. Res.*, 2009, **42**, 135–145.

35 W. Shi, X. Liu, T. Deng, S. Huang, M. Ding, X. Miao, C. Zhu, Y. Zhu, W. Liu, F. Wu, C. Gao, S. W. Yang, H. Y. Yang, J. Shen and X. Cao, Enabling Superior Sodium Capture for Efficient Water Desalination by a Tubular Polyaniline Decorated with Prussian Blue Nanocrystals, *Adv. Mater.*, 2020, **32**(33), e1907404.

36 M.-L. Liu, L. Li, M.-J. Tang, L. Hong, S.-P. Sun and W. Xing, Multi-component separation of small molecular/ionic pollutants with smart pH-gating membranes, *Chem. Eng. Sci.*, 2021, **245**, 116854.

37 S. Zhao, Z. Wang, J. Wang, S. Yang and S. Wang, PSf/PANI nanocomposite membrane prepared by *in situ* blending of PSf and PANI/NMP, *J. Membr. Sci.*, 2011, **376**(1–2), 83–95.

38 L. L. Xu, K. P. Wang, K. L. Li, S. Y. Zhao and J. Wang, Development and performance of stable PANI/MWNT conductive membrane for contaminants degradation and anti-fouling behavior, *Sep. Purif. Technol.*, 2022, **282**, 120112.

39 D. Li and R. B. Kaner, Shape and Aggregation Control of Nanoparticles: Not Shaken, Not Stirred, *J. Am. Chem. Soc.*, 2005, **128**, 968–975.

40 Y. J. Lim, J. Lee, T.-H. Bae, J. Torres and R. Wang, Feasibility and performance of a thin-film composite seawater reverse osmosis membrane fabricated on a highly porous microstructured support, *J. Membr. Sci.*, 2020, **611**, 118407.

41 X. Zhang, Y. Lv, H. C. Yang, Y. Du and Z. K. Xu, Polyphenol Coating as an Interlayer for Thin-Film Composite Membranes with Enhanced Nanofiltration Performance, *ACS Appl. Mater. Interfaces*, 2016, **8**(47), 32512–32519.

42 F. Y. Zhao, Y. L. Ji, X. D. Weng, Y. F. Mi, C. C. Ye, Q. F. An and C. J. Gao, High-Flux Positively Charged Nanocomposite Nanofiltration Membranes Filled with Poly(dopamine) Modified Multiwall Carbon Nanotubes, *ACS Appl. Mater. Interfaces*, 2016, **8**(10), 6693–6700.

43 Z. Y. Ma, X. Zhang, C. Liu, S. N. Dong, J. Yang, G. P. Wu and Z. K. Xu, Polyamide nanofilms synthesized *via* controlled interfacial polymerization on a "jelly" surface, *Chem. Commun.*, 2020, **56**(53), 7249–7252.

44 Z. Zhang, X. Shi, R. Wang, A. Xiao and Y. Wang, Ultra-permeable polyamide membranes harvested by covalent organic framework nanofiber scaffolds: a two-in-one strategy, *Chem. Sci.*, 2019, **10**(39), 9077–9083.

45 X. Song, Y. Zhang, H. M. Abdel-Ghafar, E.-S. A. Abdel-Aal, M. Huang, S. Gul and H. Jiang, Polyamide membrane with an ultrathin GO interlayer on macroporous substrate for minimizing internal concentration polarization in forward osmosis, *Chem. Eng. J.*, 2021, **412**, 128607.

46 J.-J. Wang, H.-C. Yang, M.-B. Wu, X. Zhang and Z.-K. Xu, Nanofiltration membranes with cellulose nanocrystals as an interlayer for unprecedented performance, *J. Mater. Chem. A*, 2017, **5**(31), 16289–16295.

47 J. Yuan, M. Wu, H. Wu, Y. Liu, X. You, R. Zhang, Y. Su, H. Yang, J. Shen and Z. Jiang, Covalent organic framework-modulated interfacial polymerization for ultrathin desalination membranes, *J. Mater. Chem. A*, 2019, **7**(44), 25641–25649.

48 C. Jiang, L. Tian, Z. Zhai, Y. Shen, W. Dong, M. He, Y. Hou and Q. J. Niu, Thin-film composite membranes with aqueous template-induced surface nanostructures for enhanced nanofiltration, *J. Membr. Sci.*, 2019, **589**, 117244.

49 J. Zhu, S. Yuan, A. Uliana, J. Hou, J. Li, X. Li, M. Tian, Y. Chen, A. Volodin and B. V. der Bruggen, High-flux thin film composite membranes for nanofiltration mediated by a rapid co-deposition of polydopamine/piperazine, *J. Membr. Sci.*, 2018, **554**, 97–108.

50 X. Zhu, Z. Yang, Z. Gan, X. Cheng, X. Tang, X. Luo, D. Xu, G. Li and H. Liang, Toward tailoring nanofiltration performance of thin-film composite membranes: novel insights into the role of poly(vinyl alcohol) coating positions, *J. Membr. Sci.*, 2020, **614**, 118526.

51 Z. Wang, W. Fang, F. Zhang, Y. Zhu and J. Jin, Ultrathin Nanofiltration Membrane from Confined Polymerization within the Nanowire Network for High Efficiency Divalent Cation Removal, *ACS Macro Lett.*, 2019, **8**(10), 1240–1246.

52 S. Gao, Y. Zhu, Y. Gong, Z. Wang, W. Fang and J. Jin, Ultrathin Polyamide Nanofiltration Membrane Fabricated on Brush-Painted Single-Walled Carbon Nanotube Network Support for Ion Sieving, *ACS Nano*, 2019, **13**(5), 5278–5290.

53 X. Zhu, X. Cheng, X. Luo, Y. Liu, D. Xu, X. Tang, Z. Gan, L. Yang, G. Li and H. Liang, Ultrathin Thin-Film Composite Polyamide Membranes Constructed on Hydrophilic Poly(vinyl alcohol) Decorated Support Toward Enhanced Nanofiltration Performance, *Environ. Sci. Technol.*, 2020, **54**(10), 6365–6374.

This journal is © The Royal Society of Chemistry 2022

J. Mater. Chem. A, 2022, **10**, 4392–4401 | **4401**